RSC Advances

PAPER

View Article Online
View Journal | View Issue



Cite this: *RSC Adv.*, 2026, **16**, 4788

# MnFe aminoclay as a novel catalyst: structural characterization and potential for catechol detection

Hai Le Tran,[abcde] Kieu Tran Thi Thuy,[a] Luan Thanh Nguyen,[ace] Viet Quoc Nguyen,[ace] Tin Chanh Duc Doan,[bcd] Van-Quy Hoang,[f] Thi H. Ho[gh] and Vu Khac Hoang Bui[*ij]

The development of enzyme-mimicking nanomaterials offers a promising route toward sensitive, stable, and cost-effective detection of phenolic compounds. In this study, MnFe hybrid aminoclay (MnFeAC) was synthesized and systematically characterized by XRD, XPS, SEM, TEM, and elemental mapping to confirm its amorphous structure, homogeneous elemental distribution, and mixed-valence states of Mn and Fe that underpin its catalytic activity. The MnFeAC material exhibited oxidase-like properties, enabling the oxidation of catechol in the presence of 4-aminoantipyrine (4-AAP) with a distinct colorimetric signal at 510 nm. Under optimized conditions, a linear calibration curve was obtained in the range of 1–100 μM with high correlation and sensitivity. A key advantage of our method is that no external $H_2O_2$ was required, avoiding issues of toxicity, instability, and handling hazards associated with hydrogen peroxide. Furthermore, the MnFeAC-catalyzed system maintained stable signal intensity without significant interference from $H_2O_2$ concentration effects, highlighting its intrinsic oxidase-like activity. While this preliminary study demonstrates a proof-of-concept for MnFeAC as an oxidase mimic for catechol detection, further optimization of nanomaterial composition, reaction conditions, and assay design is needed to improve detection limits and extend the method to broader classes of phenolic pollutants. These findings provide a foundation for developing hybrid aminoclay-based nanozymes as safe and effective sensing platforms for environmental monitoring applications.

Received 15th October 2025
Accepted 2nd January 2026

DOI: 10.1039/d5ra07889j

rsc.li/rsc-advances



## 1. Introduction

Phenolic compounds are widely used in chemical, pharmaceutical, and petrochemical industries, but their release into the environment poses serious risks due to toxicity, persistence, and bioaccumulation.[1,2] Rapid detection and efficient removal of phenols remain critical challenges. Among them, catechol (1,2-dihydroxybenzene) is an important representative that is extensively applied as a precursor in the manufacture of pesticides, pharmaceuticals, and fine chemicals, as well as in the photography and fragrance industries. Catechol has a molecular weight of 110.11 g $mol^{-1}$, a $pK_a$ of 9.45, and relatively high solubility in water (312 g $L^{-1}$ at 20 °C), which favors its mobility in aqueous environments. It exhibits a characteristic UV-vis absorption maximum at 275 nm, making it a model compound for spectrophotometric monitoring. Despite its industrial utility, catechol is considered hazardous, with an $LD_{50}$ of ~300 mg $kg^{-1}$ (oral, rat), indicating significant acute toxicity. In addition, its aromatic structure and resistance to biodegradation contribute to environmental persistence and potential ecological risks.[1,3–5] Therefore, sensitive, rapid, and reliable detection of catechol is not only necessary for

[a]Ho Chi Minh City University of Technology (HCMUT), 268 Ly Thuong Kiet Street, Dien Hong Ward, Ho Chi Minh City, Vietnam
[b]University of Science (HCMUS), 227 Nguyen Van Cu Street, Cho Quan Ward, Ho Chi Minh City, Vietnam
[c]Viet Nam National University Ho Chi Minh City, Vo Truong Toan Street, VNU-HCM Urban Area, Quarter 33, Linh Xuan Ward, Ho Chi Minh City, Vietnam
[d]Advanced Materials Technology Institute (AMTI), Vo Truong Toan Street, VNU-HCM Urban Area, Quarter 33, Linh Xuan Ward, Ho Chi Minh City, Vietnam
[e]Key Laboratory for Polymer and Composite Materials, Viet Nam National University Ho Chi Minh City, 268 Ly Thuong Kiet Street, Dien Hong Ward, Ho Chi Minh City, Vietnam
[f]Center for Environmental Intelligence, College of Engineering and Computer Science, VinUniversity, Gia Lam District, Hanoi 14000, Vietnam. E-mail: quy.hv@vinuni.edu.vn
[g]Laboratory for Computational Physics, Institute for Computational Science and Artificial Intelligence, Van Lang University, Ho Chi Minh City, Vietnam. E-mail: thi.hohuynh@vlu.edu.vn
[h]Faculty of Mechanical – Electrical and Computer Engineering, Van Lang School of Technology, Van Lang University, Ho Chi Minh City, Vietnam
[i]Laboratory for Advanced Nanomaterials and Sustainable Energy Technologies, Institute for Computational Science and Artificial Intelligence, Van Lang University, Ho Chi Minh City, Vietnam. E-mail: vu.buikhachoang@vlu.edu.vn
[j]Faculty of Applied Technology, Van Lang School of Technology, Van Lang University, Ho Chi Minh City, Vietnam

environmental monitoring but also critical for guaranteeing human and ecological safety.

Among the various detection strategies, colorimetric methods have attracted considerable attention owing to their simplicity, rapid response, compatibility with on-site detection, and low cost.[2,6] Colorimetric platforms often rely on the oxidation of phenolic substrate into chromogenic products, a reaction typically catalyzed by natural enzymes such as laccase, tyrosinase, and peroxidase.[7–10] However, their application is constrained by low stability under harsh conditions, high production costs, and difficulties in recycling.[2,11] These limitations have driven research into abiotic nanozymes–nanomaterials capable of mimicking enzymatic redox transformations with higher tunability, stability and scalability.[2,6,12–14] Nanozymes have expanded into diverse classes such as metal oxides, metal nanoparticles, carbon-based materials, metal–organic frameworks (MOFs), and transition-metal hybrids, each offering distinct catalytic pathways and substrate selectivity.[2,6,14–20] Notably, many nanozymes exhibit exceptional stability, retaining catalytic activity across broad pH ranges, high ionic strength, and elevated temperatures where natural enzymes rapidly deactivate.[18] Their surface-dependent electronic structures also allow precise modulation of active sites, enabling rational design of catalytic performance through defect engineering, redox pairing, heteroatom incorporation, and nanosheet confinement.[17,19] Moreover, nanozymes can also be conveniently separated from the medium for further utilization and integrated into solid supports or sensing platforms without complex immobilization procedures.[13,18] These advantages position nanozymes as highly promising alternatives for phenolic compound detection, where rapid electron-transfer reactions and substrate oxidation are essential for achieving sensitive colorimetric readouts.

Aminoclays (ACs) are organic–inorganic hybrids with dispersible two-dimensional silicate frameworks functionalized by amino groups.[21] Their solubility in water, abundant surface functionalities, and ability to stabilize transition metals make them attractive support for catalysis and sensing.[22–24] Specifically, CoAC and MgAC-$Fe_3O_4$/$TiO_2$ have been applied as nanozymes for the detection of glucose and phenolic compounds, respectively.[25,26] However, monometallic aminoclay itself has low catalytic activity and is frequently combined with other materials to enhance its catalytic efficiency.[23,27–29] This strategy raises concern about the production cost, complexity in production, and low scalability potential. Recently, bimetallic aminoclays have been introduced to replace the conventional monometallic aminoclays.[13,30,31] For instance, Zeng *et al.* (2024) constructed CuMn aminoclays (CuMnACs) with pronounced laccase-like activity, demonstrating superior catalytic oxidation of bisphenol A (BPA) compared to natural laccases. The synergistic interplay of Cu and Mn redox pairs not only enhanced catalytic efficiency but also enabled high stability and recyclability. Their mechanistic investigation revealed that both non-radical $Mn^{3+}$-mediated oxidation and radical pathways involving $O_2^{\bullet-}$ and $^1O_2$ were responsible for BPA oxidation. Importantly, CuMnAC-1–7 achieved rapid BPA removal (95% within 1 h), underscoring the potential of Mn-based aminoclay systems as robust laccase-mimicking nanozymes for phenolic pollutant remediation.[13] Similarly, Mahadevaprasad *et al.* (2024) developed a novel Fe–Zr hybrid aminoclay (FeZrAC) incorporated into a biopolymer-based thin film composite (TFC) membrane for pollutant remediation. The Fe–Zr redox centers acted synergistically with $H_2O_2$ to generate reactive species, enabling ultrafast degradation of dyes and organic pollutants within 4 min. The optimized FZ-TFC-1 membrane achieved nearly complete pollutant removal (>95%) while maintaining high water flux (>67 L $m^{-2}$ $h^{-1}$). Importantly, the membrane showed exceptional antifouling and self-cleaning performance, sustaining activity for up to 150 h with negligible Fe/Zr leaching. Mechanistic studies revealed that $Fe^{2+}/Fe^{3+}$ cycling and $Zr^{4+}$ sites cooperatively promoted hydroxyl ($^{\bullet}OH$) and hydroperoxyl ($^{\bullet}OOH$) radical generation, accelerating degradation pathways.[30]

Although recent studies have demonstrated the potential of hybrid aminoclays for pollutant remediation, important limitations remain. For example, CuMnACs exhibit strong laccase-like activity for bisphenol A degradation,[13] yet the use of copper raises concerns about toxicity and possible environmental risks.[32] Likewise, FeZrAC membranes have ultrafast degradation efficiency,[30] but the inclusion of zirconium significantly increases the production cost and challenges scalability.[33] To overcome these issues, we propose the use of MnFe hybrid aminoclay (MnFeAC), which integrates two earth-abundant and relatively low-toxicity metals. By eliminating Cu and Zr, MnFeAC strikes a balance between catalytic activity, environmental safety, and economic feasibility. In addition, their facile and low-cost synthesis makes them particularly attractive for sensitive phenolic compound detection, providing a sustainable alternative to previous aminoclay systems.

In this study, MnFeAC was synthesized and systematically characterized to explore its potential as an abiotic oxidase-like nanozyme for phenolic compound detection. Morphological and structural analyses by XRD, XPS, SEM, and TEM revealed that the material consisted of ultrathin, partially amorphous nanosheets with uniformly distributed $Mn^0$ and $Fe^0$ within the silicate framework. These characteristics collectively suggest a material with high surface exposure, homogeneous metal dispersion, and flexible redox activity—features favorable for facilitating electron transfer and catalytic oxidation. Building on these physicochemical properties, this work evaluates the MnFeAC as a simple, stable, and environmentally benign colorimetric platform for the peroxide-free detection of catechol as a model phenolic compound.

## 2. Experimental

### 2.1. Chemical and materials

All reagents used in this study were of analytical grade and were utilized as received, without further purification. Manganese(II) chloride tetrahydrate ($MnCl_2 \cdot 4H_2O$), iron chloride hexahydrate ($Fe(Cl)_3 \cdot 6H_2O$), and aminopropyltriethoxysilane (APTES) were selected as precursors of MnFeAC. Catechol ($C_6H_6O_2$) was used as a model phenolic compound. Aminoantipyrine (4-AAP) was applied as a probe for the screening of enzyme-like activity and

the detection of catechol.[13,34] For this study, all chemicals were supplied by Sigma-Aldrich (USA), and experiments were conducted using deionized (DI) water with a resistivity of 18.25 MΩ cm.

### 2.2. Synthesis of MnFe aminoclay

ACs were synthesized following the procedure outlined by earlier studies.[27] Specifically, 41.67 mM of metal salts with varying Mn/Fe molar ratios (Table 1) were dissolved in 200 mL of EtOH, after which 56.3 mM APTES was introduced. The solution was stirred for 8 hours to yield a homogeneous suspension. The suspension was subsequently centrifuged at 3500 rpm for 15 min and rinsed with ethanol to eliminate residual impurities. The obtained product was dried at 40 °C and finally ground into powder.

### 2.3. MnFe aminoclay as catalyst for the detection of catechol

**2.3.1. Evaluation of enzyme-mimicking activity.** The enzyme-mimicking activity of the aminoclay was evaluated using a catechol/4-aminoantipyrine (4-AAP) chromogenic system. Briefly, 500 μL of catechol solution (1.0 mg $mL^{-1}$, 9.08 mM), 500 μL of 4-AAP solution (1.0 mg $mL^{-1}$), and 500 μL of aminoclay suspension (1.0 mg $mL^{-1}$) were mixed with 3.5 mL of phosphate-buffered saline (PBS, pH 7.4). The reaction mixture was incubated at 35 °C for 20 min under gentle mixing to ensure homogeneity. Following incubation, the mixture was centrifuged at 10 000 rpm for 2 min to remove any particulate matter. The absorbance of the resulting supernatant was recorded at 510 nm ($UV_{510}$), and the colorimetric response was used to assess the enzyme-like catalytic activity of the aminoclay.[13]

**2.3.2. Optimization of MnFeAC for the detection of phenolic compounds.** The detection performance of MnFe aminoclay (MnFeAC) was systematically optimized under various experimental conditions. MnFeAC with an optimal Mn : Fe molar ratio of 5 : 1 was employed as the catalyst. The effect of catalyst dosage was examined within the range of 0.01–0.20 mg $mL^{-1}$, while the solution pH was adjusted between 3.0 and 9.0. Reaction time varied at 20, 40, and 60 min to evaluate kinetic influences. Temperature-dependent experiments were conducted at 35 °C and 45 °C to assess thermal effects. The effects of 4-AAP and $H_2O_2$ concentration were also considered. These optimization parameters were selected to identify the most favorable conditions for enhancing the sensitivity and reproducibility of phenolic compound detection.

Table 1 List of synthesized samples

| Sample | $MnCl_2 \cdot 4H_2O$ (mM) | $Fe(Cl)_3 \cdot 6H_2O$ (mM) | APTES (mM) |
|---|---|---|---|
| MnAC | 41.67 | 0 | 56.3 |
| MnFe AC 1 : 3 | 10.42 | 31.25 | |
| MnFe AC 1 : 1 | 20.84 | 20.84 | |
| MnFe AC 3 : 1 | 31.25 | 10.42 | |
| MnFe AC 5 : 1 | 34.73 | 6.94 | |
| MnFe AC 7 : 1 | 36.46 | 5.21 | |
| FeAC | 0 | 41.67 | |

**2.3.3. Catalytic kinetic parameters of MnFeAC.** The kinetic analysis method was conducted using varying concentrations of catechol (1–1000 μM), which were reacted with 4-AAP in PBS buffer (pH = 7.4). All kinetic experiments were carried out at 45 °C. $K_m$ and $v_{max}$ were determined using the Michaelis–Menten equation (eqn (1)) to evaluate nanozyme activity:

$$v = \frac{v_{max} \times [S]}{K_m + [S]} \quad (1)$$

where $K_m$ represents the Michaelis–Menten constant, $v_{max}$ is the initial maximum reaction rate, while $v$ and [S] denote the initial reaction rate and substrate concentration, respectively. The molar absorption coefficient of the reaction product was taken as 13.6 $mM^{-1}$ $cm^{-1}$.[2]

**2.3.4. LOQ/LOD for the detection of catechol.** The analytical performance of MnFeAC was further evaluated by determining the limit of detection (LOD) and limit of quantification (LOQ) for catechol. A series of catechol standard solutions in the concentration range of 1–100 μM were prepared and reacted under the optimized conditions established in Section 2.3.2. The absorbance values at 510 nm were recorded and used to construct a calibration curve. The LOD and LOQ were calculated based on the standard deviation of the blank response ($\sigma$) and the slope of the calibration curve ($S$), using the following formulas (eqn (2) and (3)).[35]

$$\mathrm{LOD} = \frac{3.3 \times \sigma}{S} \quad (2)$$

$$\mathrm{LOQ} = \frac{10 \times \sigma}{S} \quad (3)$$

where $\sigma$ is the standard deviation of the blank signal and $S$ is the slope of the calibration curve.

**2.3.5. Preliminary analysis of real samples.** The laboratory tap water was initially filtered using a 0.45 μm filter, and it was adjusted to approximately 7.4 prior to analysis. A known volume of standard concentration catechol solution was then added to the actual sample. The previously described colorimetric method was applied to these real samples for further analysis.[2,16] To calculate the recovery rate (%) and relative standard deviation (RSD), the following formulas were applied (eqn (4) and (5)):[20]

$$\mathrm{Recovery}(\%) = \frac{C_{measured} - C_{unspiked}}{C_{added}} \times 100 \quad (4)$$

$$\mathrm{RSD}(\%) = \frac{\text{standard deviation}}{\text{mean}} \times 100 \quad (5)$$

### 2.4. Characterization techniques

The morphology and surface features of the MnFe aminoclay were examined using scanning electron microscopy (SEM, Hitachi S-4800, Japan), while nanoscale structural details were obtained by transmission electron microscopy (TEM, JEM-2100). Selected area electron diffraction (SAED) patterns were collected to evaluate crystallinity and Energy-dispersive X-ray spectroscopy (EDS) coupled with elemental mapping was employed to determine the elemental composition and spatial

 

distribution of Mn, Fe, Si, O, and N within the hybrid framework. To further elucidate the structural order, X-ray diffraction (XRD, D8 Advance, Bruker, USA) was carried out to probe phase composition and crystalline, with particular attention to the absence or broadening of characteristic reflections, which is consistent with a semi-amorphous state. Additionally, X-ray photoelectron spectroscopy (XPS, Shimadzu AXIS Ultra DLD, Japan) was employed to analyze the surface chemical states of Mn and Fe, providing insights into their oxidation states and confirming their successful incorporation into the aminoclay matrix. BET surface area, pore size, and pore volume of obtained materials were investigated using Nova Station A (Anton Paar, Austria). Together, these complementary techniques provided a comprehensive understanding of the morphology, structure, and surface chemistry of the MnFe aminoclay.

### 2.5. Statistical analysis

All experiments were carried out in triplicate, and data are reported as mean ± standard deviation (SD). Group comparisons were performed using one-way analysis of variance (ANOVA) followed by Tukey's *post-hoc* test to determine significant pairwise differences. A significance threshold of $p < 0.05$ was applied for all analyses. Statistical calculations were performed using OriginPro 2021.

## 3. Result and discussion

### 3.1. Characterization of MnFeAC

The XRD patterns of MnFeAC (5 : 1), MnAC, and FeAC (Fig. 1) reveal significant differences in structural ordering among the samples. The FeAC sample exhibited several sharp diffraction peaks, indicating a highly crystalline structure. The main reflections at approximately $2\theta = 9.4°$, 18.8°, 28.6°, 33.4°, 36.1°, 45.3°, and 60.2° could not be assigned to common iron oxide phases such as α-$Fe_2O_3$ or γ-$Fe_2O_3$ but were closed to the characteristic peaks of $Fe_2SiO_4$ (JCPDS No. 77-1667).[36,37] This confirms that $Fe^{3+}$ ions were incorporated into the silicate network, forming an ordered Fe–O–Si framework rather than segregated iron oxide crystallites. The presence of low-angle reflections (~9° and 18°) further supports the layered nature of the Fe-aminoclay structure. In contrast, the MnAC sample exhibited a series of weak and broadened peaks centered around $2\theta$ = 28–38°, which can be indexed to the planes of $Mn_3O_4$ (JCPDS No. 80-0382), suggesting the formation of poorly crystalline hausmannite-type $Mn_3O_4$ domains.[38] The relatively broad diffraction peaks indicate short-range ordering and nanoscale crystallite size, typical for sol–gel-derived manganese aminoclays. Notably, MnFeAC (5 : 1) presented a featureless broad pattern without distinct reflections, confirming its predominantly amorphous structure.[27] This progressive reduction in crystallinity from FeAC to MnAC and finally to MnFeAC highlights the strong influence of Mn incorporation, and especially the synergistic Mn–Fe interaction, in suppressing long-range crystallization. The formation of an amorphous framework in MnFeAC is expected to generate abundant defect sites and unsaturated coordination environments, which can provide favorable active sites for catalytic reactions compared to the more crystalline FeAC and MnAC.

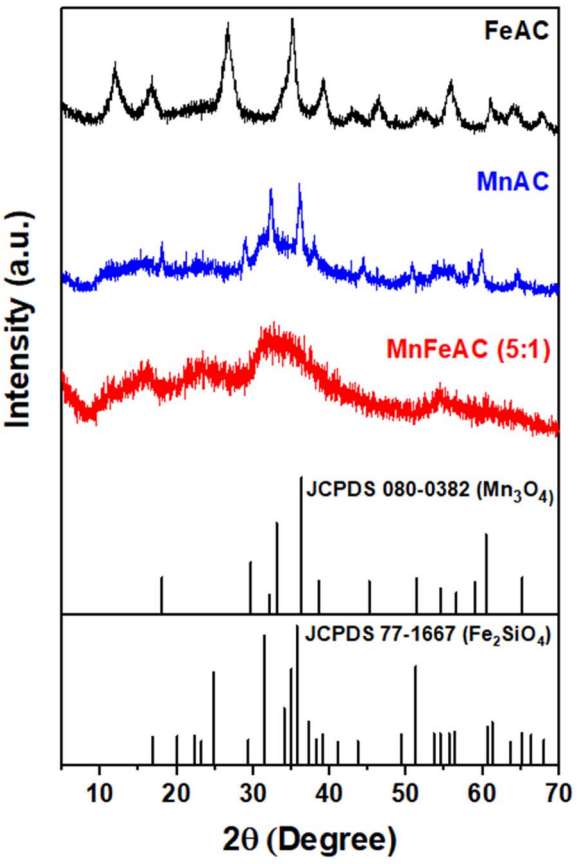


Fig. 1 XRD patterns of MnAC, FeAC, and MnFeAC (5 : 1) samples.

X-ray photoelectron spectroscopy (XPS) was employed to investigate the surface chemical composition and bonding environments of MnFeAC (5 : 1). The survey spectrum confirmed the presence of Mn, Fe, O, C, N, and Si in the obtained materials (Fig. 2). Surface atomic ratios indicate Fe (28.6 at%) is more abundant than Mn (15.3 at%), suggesting Fe enrichment at the surface. High-resolution spectra were further deconvoluted to provide detailed insights into the chemical states of each element. The C 1s spectrum displayed two components at 281.98 and 283.20 eV. Although the dominant peak at 281.98 eV is rarely discussed in the literature, it can be assigned to metal–carbon and metal–oxygen–carbon interactions (Me–C/Me–O–C), as supported by several references.[39,40] In contrast, the minor peak at 283.20 eV corresponded to C–Si bonds in the silicate framework.[31] The absence of higher-binding-energy peaks suggests minimal oxygenated carbons, confirming that the carbon environment is dominated by metal–C and C–Si linkages. The N 1s spectrum of MnFe-AC shows two peaks at 398.2 and 398.5 eV, which can be assigned to imine-type (C=N) and amine-type (C–N) nitrogen species, respectively.[31] The slight shift to lower binding energies compared to free amines suggests coordination between nitrogen atoms and transition metals (Mn/Fe). The absence of higher binding energy contributions indicates negligible oxidized nitrogen species. These results confirm that

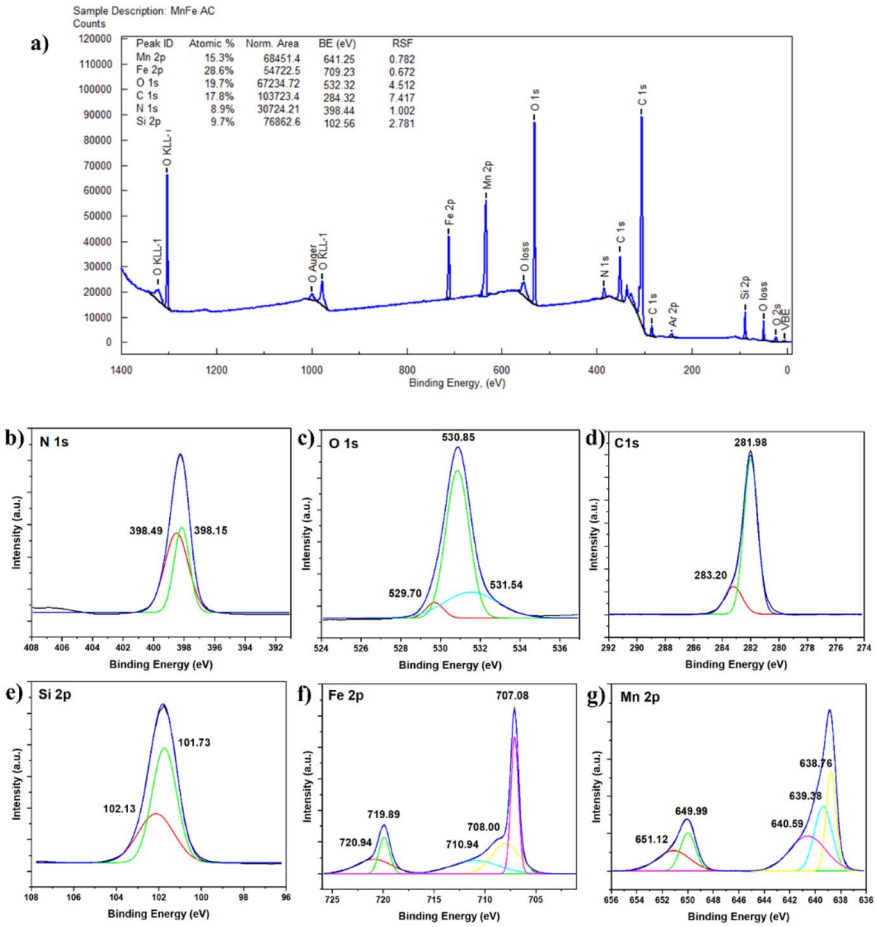


Fig. 2 XPS spectra of MnFeAC (5 : 1): survey spectrum (a); high-resolution spectra of N 1s (b), O 1s (c), C 1s (d), Si 2p (e), Fe 2p (f), and Mn 2p (g).

nitrogen exists predominantly as amine/imine groups that are chemically bonded to the inorganic framework, thereby providing anchoring sites for Mn and Fe and enhancing the electron transfer capacity of the hybrid aminoclay. The O 1s spectrum was deconvoluted into three components at 529.70, 530.85, and 531.54 eV. The peak at 529.7 eV corresponds to lattice oxygen ($O^{2-}$) in Mn–O/Fe–O bonds, while the peak at 530.85 eV is associated with Si–O–Si. The higher binding energy peak at 531.5 eV was assigned to adsorbed oxygen species ($O_{ads}$) and Si–O– groups.[41,42] The Si 2p spectrum of MnFe-AC displays two components at 101.7 and 102.1 eV, corresponding to Si–C and Si–O–Si/Si–O–C bonds, respectively.[43,44] The presence of both organic (Si–C) and inorganic (Si–O–Si) linkages confirms the hybrid nature of the aminoclay framework. These chemical environments provide anchoring sites for Mn and Fe species and enhance the structural stability of the composite. The Fe 2p spectrum of MnFe-AC reveals multiple contributions. The peaks at 708.0 eV can be assigned to $Fe^0/Fe^{2+}$ species, while the component at 710.9 eV corresponds to $Fe^{3+}$.[6,45,46] These results demonstrate that Fe exists in a mixed-valence state ($Fe^{2+}/Fe^{3+}$), which is known to facilitate electron transfer processes and enhance catalytic activity. The low-BE component at 707.1 eV may also indicate strong metallic $Fe^0$ or Fe–C/Fe–Si interactions within the aminoclay framework, consistent with the C 1s analysis.[39,46–49] The Mn 2p spectrum of MnFeAC exhibits deconvoluted peaks at 638.8, 639.4, and 640.6 eV in the Mn $2p_{3/2}$ region, along with spin–orbit components at 650.0 and 651.1 eV. The peaks at 640.6 eV and 651.1 eV is characteristic of $Mn^{2+}$,[13,16,46] while the lower-BE components (638.8 and 639.4 eV) suggest reduced Mn environments, possibly arising from metallic $Mn^0$, Mn–C or Mn–Si bonding in the aminoclay framework.[46,49] The absence of significant high-BE components (>641.5 eV) indicates that $Mn^{3+}/Mn^{4+}$ species are negligible.[13,16,46] These results demonstrate that Mn is predominantly present in reduced states ($Mn^{2+}$ and sub-oxidized Mn), which are known to enhance electron transfer and redox activity in catalytic systems. XPS analysis confirmed that MnFe-AC possesses a hybrid organic–inorganic framework with Mn and Fe anchored through strong C–Si, C–N, and metal–C interactions. Both Fe and Mn exist in mixed/reduced valence states (Feo/$Fe^{2+}/Fe^{3+}$ and $Mn^0/Mn^{2+}$), while oxygen species are distributed among lattice oxygen, Si–O–Si sites, and adsorbed groups. The coexistence of redox-active metals and surface oxygen functionalities highlights a synergistic environment that facilitates electron transfer and reactive oxygen species generation. These surface characteristics provide strong evidence that MnFeAC is structurally and chemically optimized for catalytic applications.

The morphology of MnFeAC (5 : 1) was investigated using SEM, TEM, SAED, and EDS elemental mapping. SEM micrographs revealed irregular, porous aggregates with rough surfaces, typical of the hybrid organic–inorganic aminoclay matrix (Fig. 3a1). At higher magnifications, the material appeared as loosely packed nanoparticles without distinct crystalline facets, suggesting that Mn and Fe were dispersed within the aminoclay framework rather than forming large crystalline particles (Fig. 3a2). SEM–EDS elemental mapping confirmed the homogeneous distribution of C, N, Si, O, Fe, and Mn throughout the sample. Carbon and nitrogen were evenly distributed, consistent with the aminoclay organic backbone, while silicon and oxygen were uniformly present as part of the silicate framework (Fig. S1). TEM analysis provided further insight into the nanostructure, with darker $Mn^0/Fe^0$-rich domains observed embedded in a lighter aminoclay background (Fig. 3b1), while high-resolution TEM suggested the presence of ultra-small nanodomains (2–10 nm) dispersed throughout an amorphous matrix. The selected area electron diffraction (SAED) pattern displayed a broad diffuse halo with faint rings, confirming the predominantly amorphous nature of the material with only short-range order and nanocrystalline clusters, consistent with the XRD and XPS results (Fig. 3b2).

Taken together, these results demonstrate that MnFe AC (5 : 1) possesses a hybrid amorphous–nanocrystalline structure, in which highly dispersed $Mn^0/Fe^0$ domains are stabilized within the silicate–aminoclay framework. This structural configuration provides a high density of accessible surface sites and prevents the formation of inactive aggregates, features that are expected to enhance catalytic performance.

Nitrogen sorption analyses reveal that MnAC, FeAC, and MnFeAC (5 : 1) all exhibit Type II isotherms with H3 hysteresis loops (Fig. S2), confirming that these aminoclays possess a predominantly nonporous layered structure with only minor slit-like voids generated by sheet stacking. All materials showed low surface area and pore volumes (Table S1) with notable differences exist among them. FeAC displays the highest BET surface area (5.07 $m^2\ g^{-1}$) and the largest mesopore volume ($0.015\ cm^3\ g^{-1}$) with a broader pore size distribution centered at 2-5 nm. In contrast, MnAC and MnFeAC (5 : 1) have surface areas below 1 $m^2\ g^{-1}$ and pore volumes of only $\sim$0.002 $cm^3\ g^{-1}$. The negligible microporosity observed across all samples confirmed that these aminoclays function as essentially nonporous solids.

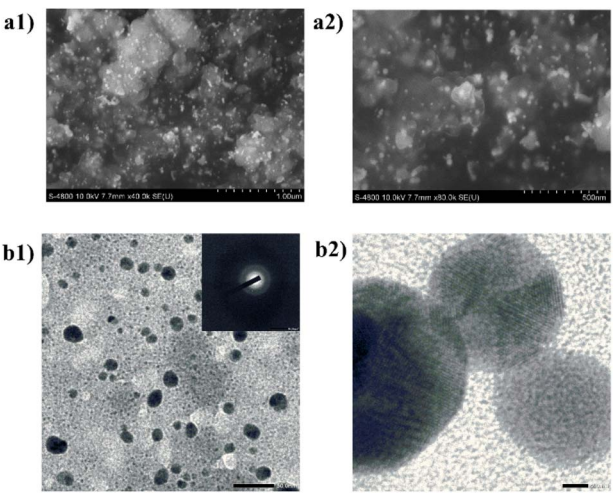


Fig. 3 SEM (a) and TEM (b) images of MnFe AC (5 : 1).

### 3.2. Evaluation of enzyme-mimicking activity

The enzyme-like catalytic performance of MnFeACs was assessed using the catechol/4-AAP chromogenic system, where the oxidative coupling reaction produces a quinone-imine dye with maximum absorbance near 510–520 nm.[6] This colorimetric response arises from MnFeAC-mediated oxidation of catechol to phenoxy/semiquinone radicals, which subsequently couple with 4-AAP to form the stable chromophore. Fig. 4a presents the UV-vis spectra of MnFeACs with different Mn : Fe molar ratios compared to single-metal aminclays (MnAC and FeAC). MnAC showed moderate activity, while FeAC exhibited relatively low catalytic responses, indicating limited enzyme-mimicking activity when used individually. In contrast, MnFeACs demonstrated significantly higher absorbance in the visible region, confirming enhanced oxidative activity upon incorporation of both Mn and Fe. Interestingly, the catalytic performance follows the opposite trend in surface area, where FeAC has the highest surface area. This clear lack of correlation between porosity and catalytic behavior demonstrated that textural properties do not govern the nanozyme activity of aminoclays. Instead, the superior performance of MnFeAC arises from intrinsic electronic factors, specifically the synergistic redox interplay between $Mn^{2+}/Mn^{3+}$ and $Fe^{2+}/Fe^{3+}$ centers, which promotes more efficient electron transfer and faster catalytic cycling than in monometallic aminoclays.

Among the MnFeAC formulations tested, increasing Mn content correlated with larger $UV_{510}$ responses, with MnFeAC(5 : 1) yielding the highest response, while MnFeAC (7 : 1) and MnFeAC (3 : 1) showed slightly lower absorbance values (Fig. 4b). Statistical analysis (one-way ANOVA) indicated significant overall differences among the three groups ($p < 0.05$). However, *post-hoc* comparisons revealed that MnFeAC (5 : 1) and MnFeAC (7 : 1) were not significantly different from each other ($p > 0.05$), whereas both performed significantly better than MnFeAC (3 : 1). These results suggest that MnFe AC exhibits a broad optimum in Mn-rich compositions, with maximal or near-maximal performance achieved at Mn : Fe ratios between 5 : 1 and 7 : 1. Zeng *et al.* (2024) also reported that Mn-rich bimetallic CuMnACs exhibited the highest activity in bisphenol A (BPA) oxidation due to the efficient electron exchange between $Cu^{2+}/Cu^{+}$ and $Mn^{4+}/Mn^{3+}$.[13] Although the differences were not large, MnFe AC (5 : 1) was selected for subsequent experiments due to its highest mean activity and consistent reproducibility (smaller error bars).

### 3.3. Optimization of MnFeAC for the detection of phenolic compounds

**3.3.1. Catalyst dosage.** The influence of MnFeAC (5 : 1) dosage on the colorimetric response toward catechol was

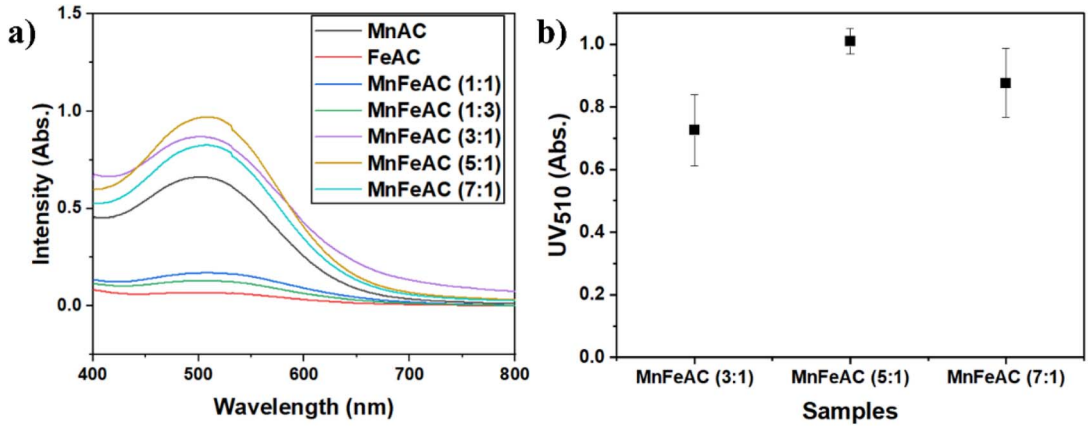


Fig. 4 Colorimetric response of MnFeAC catalysts with different Mn : Fe ratios: (a) UV-vis spectra of aminoclay-based catalysts; (b) comparison of $UV_{510}$ for MnFeAC (3 : 1), MnFeAC (5 : 1), and MnFeAC (7 : 1), respectively. Experiments were performed in triplicate ($n = 3$). Error bars indicate the standard deviation (SD).

examined in the range of 0–0.20 mg $mL^{-1}$ (Fig. 5a). The absorbance at 510 nm increased sharply with increasing catalyst concentration up to 0.10 mg $mL^{-1}$, reaching a maximum value of ~1.05. Beyond this point, further increases in dosage (0.15–0.20 mg $mL^{-1}$) produced only minor changes, with absorbance values remaining close to the plateau level. One-way ANOVA confirmed significant differences among the lower dosages (0.01–0.10 mg $mL^{-1}$, $p < 0.05$), but no statistically significant difference was observed among the higher loadings (0.10, 0.15, and 0.20 mg $mL^{-1}$, $p > 0.05$). This indicates that catalyst concentrations above 0.10 mg $mL^{-1}$ do not provide additional benefit within experimental variance.

The observed trend suggests that increasing catalyst loading enhances the number of redox-active sites available for catechol oxidation, thereby promoting the generation of phenolic radicals and subsequent coupling with 4-AAP to form the quinone-imine dye. At higher concentrations, however, the signal intensity stabilized, likely due to substrate limitation or diffusion constraints rather than catalyst availability. Based on these results, 0.10 mg $mL^{-1}$ was selected as the optimal dosage for subsequent experiments, as it provided the highest absorbance with good reproducibility while minimizing the potential for background scattering or non-specific reactions at higher concentrations.

**3.3.2. pH.** The catalytic activity of MnFeAC (5 : 1) toward catechol oxidation was strongly dependent on solution pH (Fig. 5b). At acidic pH 3.0, the absorbance at 510 nm was minimal, indicating poor radical generation and limited coupling with 4-AAP. Activity increased sharply at pH 5.0 and continued to increase moderately at pH 7.4 (~1.0). The highest response was obtained under alkaline conditions at pH 9.0, although the associated error bars were larger, suggesting decreased reproducibility. One-way ANOVA confirmed a statistically significant effect of pH on the colorimetric response ($p < 0.01$). *Post-hoc* analysis showed that activity at pH ≥ 5 was significantly higher than at pH 3.0, but no significant difference was detected among pH 5.5, 7.4, and 9.0 ($p > 0.05$). These results indicate that MnFeAC (5 : 1) maintains robust enzyme-like activity across a broad near-neutral to alkaline range.

Mechanistically, at very acidic pH (<4), the amino groups ($-NH_2$) on aminoclay are protonated to $-NH_3^+$, imparting a net positive charge to the surface.[30] Under these conditions, catalytic activity is suppressed because protonation reduces electron-donating ability, and the predominant neutral form of catechol interacts weakly with the positively charged surface. As a result, phenoxy radical generation and subsequent coupling with 4-AAP are inefficient. Once the pH rises above 4, aminoclays generally acquire a net negative charge due to deprotonation of amino and silanol groups.[30] In parallel, catechol gradually deprotonates to catecholate anions ($pK_a \approx 9.45$), which are more readily oxidized to semiquinone radicals. At near-neutral conditions (pH 5–7), this synergy between negatively charged aminoclay surfaces and partially deprotonated catechol enhances adsorption through hydrogen bonding and π–π interactions and accelerates electron transfer *via* Mn–Fe redox cycling. This explains the strong and reproducible enzyme-mimicking activity observed at pH 5.5 and 7.4. At higher alkaline conditions (≥9), while catechol is fully deprotonated and highly reactive, the strong negative charge on both the aminoclay surface and catecholate anions introduces electrostatic repulsion. This reduces effective substrate binding and, together with possible dye instability, leads to higher variability in absorbance signals. Based on these results, pH 7.4 was chosen as the working condition for subsequent assays, since it provides a balance between high activity, stability of quinone–imine dye, and good reproducibility under physiologically relevant conditions.

**3.3.3. Temperature.** The influence of temperature on MnFe AC catalytic activity was evaluated at 35, 45, and 55 °C (Fig. 5c). Statistical analysis (one-way ANOVA) confirmed that temperature had a significant effect on catalytic performance ($p < 0.05$). *Post-hoc* testing indicated that the activity at 45 °C was significantly higher than at 35 °C ($p < 0.05$), whereas no significant difference was found between 45 and 55 °C ($p > 0.05$). The enhanced activity at 45 °C likely reflects accelerated electron transfer kinetics and more efficient radical generation, whereas the decline at higher temperatures suggests thermal

 

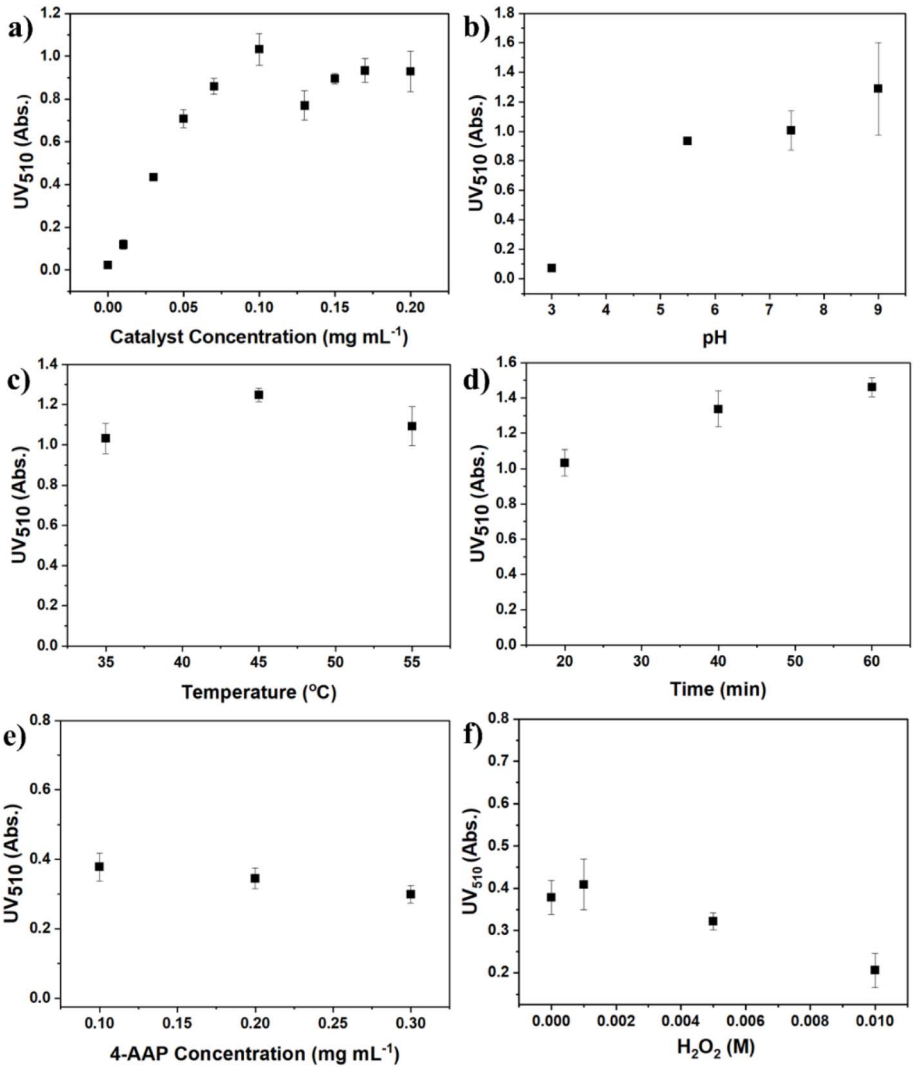


Fig. 5 Optimization of the colorimetric detection conditions using MnFeAC (5 : 1) catalyst. Effect of (a) catalyst concentration, (b) pH, (c) temperature, (d) reaction time, (e) 4-AAP concentration, and (f) $H_2O_2$ concentration on UV510. For $H_2O_2$ spiked sample, the reaction time is 10 min. Experiments were performed in triplicate ($n = 3$). Error bars indicate SD.

destabilization of the quinone–imine dye or partial deactivation of active Mn/Fe centers. Considering both sensitivity and operational stability, 45 °C was chosen as the optimal reaction temperature for subsequent experiments.

**3.3.4. Reaction time.** The catalytic response of MnFe AC toward catechol oxidation increased progressively with reaction time from 20 to 60 min (Fig. 5d). Statistical analysis (one-way ANOVA) confirmed a significant effect of time on absorbance ($p < 0.05$). *Post-hoc* comparison indicated that the 40- and 60-min values were significantly higher than 20 min, whereas the difference between 40 and 60 min was not statistically significant ($p > 0.05$). This suggests that most of the reaction is completed within the first 40 min, after which the rate slows toward equilibrium. Mechanistically, the observed increase corresponds to ongoing oxidation of catechol to phenoxy/quinone intermediates and subsequent coupling with 4-AAP. While extending the reaction time to 60 min yields a slightly higher absorbance, the marginal improvement does not outweigh the longer assay time. Therefore, 40 min was selected as the optimal reaction time, balancing assay sensitivity with practical throughput.

**3.3.5. Effect of 4-AAP concentration.** The influence of 4-aminoantipyrine (4-AAP) concentration on the colorimetric response was examined in the range of 0.10–0.30 mg $mL^{-1}$ (Fig. 5e). Interestingly, the absorbance at 510 nm decreased gradually with increasing 4-AAP concentration. This trend suggests that an excess of 4-AAP does not enhance, but rather suppresses, the formation of the quinone–imine dye. A plausible explanation is that high concentrations of 4-AAP shift the reaction equilibrium or compete with catechol radicals for active sites, thereby reducing the efficiency of coupling. In addition, excess 4-AAP may contribute to side reactions or self-absorption effects that interfere with dye development. Thus, the optimal concentration of 4-AAP for MnFe AC-mediated detection was identified as 0.10 mg $mL^{-1}$, which provided the highest absorbance signal and best signal-to-background ratio.

These findings highlight that while 4-AAP is essential as a coupling agent in the colorimetric assay, its concentration must be carefully controlled. Excess amounts can compromise sensitivity and reproducibility, underscoring the importance of reagent balance in enzyme-mimicking colorimetric systems.

Systematic optimization of experimental parameters demonstrated that the catalytic activity of MnFe AC (5 : 1) toward catechol detection depends on catalyst dosage, solution pH, reaction time, and temperature. Catalyst loading enhanced the response up to 0.10 mg $mL^{-1}$, beyond which no significant improvement was observed. The activity was strongly pH-dependent, with minimal response under acidic conditions and a broad optimum across the near-neutral to alkaline range; pH 7.4 was selected to balance activity and stability. Reaction time studies showed continuous signal growth up to 60 min, though the increase beyond 40 min was modest, and 40 min was therefore chosen for subsequent assays to improve throughput. Temperature profiling revealed a maximum response at 45 °C, with decreased activity at 55 °C, suggesting that higher temperatures compromise stability. Collectively, the optimized conditions for catechol detection were identified as MnFe AC dosage of 0.10 mg $mL^{-1}$, 4-AAP of 0.10 mg $mL^{-1}$, pH 7.4, reaction time of 40 min, and temperature of 45 °C, which provided the best balance between sensitivity, reproducibility, and operational feasibility.

### 3.4. Kinetic and detection performance of the MnFeAC-based colorimetric system for catechol

To characterize the enzyme-mimicking catalytic of MnFeAC, Michaelis–Menten was applied. The reaction rate was monitored *via* absorbance at 510 nm under various catechol concentrations from 1 to 1000 μM (Fig. 6a). The non-linear Michaelis–Menten fit yielded a $K_m$ of ~379.30 μM and $V_{max}$ of ~3.4 μM $min^{-1}$, indicating moderate substrate affinity (Fig. S3). These results confirm that MnFeAC functions effectively as a nanozyme for colorimetric catechol detection and oxidation in aqueous systems.

Based on the above optimized conditions, a calibration curve was constructed using catechol concentrations ranging from 1 to 100 μM, yielding a strong linear correlation with an $R^2$ value of 0.9978 and a sensitivity (slope) of 0.00382 (Fig. 6b). Based on the standard deviation of the blank signal, the limit of detection (LOD) and limit of quantification (LOQ) were calculated to be 0.87 μM (LOD) and 2.62 μM (LOQ) when converted to molar concentration, demonstrating that the MnFeAC-based system offers high sensitivity and reliable quantification in the low micromolar range.

Although the LOD and LOQ obtained in this study are slightly higher than those reported for some nanozyme-based systems (Table 2), a key distinction is that our assay functions effectively without the addition of hydrogen peroxide ($H_2O_2$). In many colorimetric detection platforms, $H_2O_2$ is introduced as an oxidant to enhance signal output at ~510 nm. Our results, however, demonstrate that while $H_2O_2$ significantly accelerates the reaction kinetics (reducing the detection time from ~40 min to less than 10 min), it does not increase the final absorbance intensity or improve sensitivity (Fig. 5e and S4), since the system is limited by substrate availability rather than oxidant concentration. Moreover, reliance on $H_2O_2$ introduces several drawbacks: it is unstable and decomposes during storage, requires careful handling and transport due to its corrosive and oxidative hazards, and raises safety concerns for large-scale or field applications. By contrast, the MnFeAC system directly utilizes dissolved $O_2$ as the terminal electron acceptor, eliminating the need for added $H_2O_2$. This not only simplifies the assay but also improves safety, practicality, and environmental compatibility, even if the detection limits are somewhat higher compared with $H_2O_2$-assisted assays.

To evaluate the applicability of the MnFeAC-based colorimetric system for real samples, spike-and-recovery experiments were performed using tap water. The calibration curve obtained from standard catechol solutions in deionized water was applied to estimate the concentration of catechol equivalents in tap water samples (Fig. 6b). A small background signal corresponding to approximately 3.18 μM phenol equivalents was detected in the unspiked sample, suggesting the presence of trace oxidizable organic matter or contamination during experiments. After correcting for this background, the recoveries for catechol spikes of 9.08, 45.42, and 90.84 μM were 112.3%, 113.5%, and 106.6%, respectively, with a mean recovery of 110.8 ± 3.8% (RSD = 3.4%) (Table S2). These values fall within the acceptable range (80–120%), demonstrating good accuracy and precision of the developed method in complex water matrices. After storage in PBS (pH 7.4), the catalytic activity of MnFeAC (5 : 1) was well maintained. As shown in Fig. S5, $UV_{510}$ of the detection system retained approximately ~88.7% of its initial value after two weeks, indicating negligible deactivation during storage. This excellent stability demonstrates that the aminoclay framework effectively preserves the redox-active Mn/Fe centers and prevents oxidation or aggregation during storage, which is advantageous for long-term application in colorimetric detection systems.

In addition, the potential interference effect of common inorganic ions on the colorimetric detection was evaluated by monitoring the $UV_{510}$ response in the presence of $Ca^{2+}$, $Mg^{2+}$, $NO_3^-$, and $SO_4^{2-}$.[15,18] Statistical analysis (one-way ANOVA) revealed no significant difference ($p > 0.05$) in the $UV_{510}$ response between the control and samples containing these ions, indicating that their interference effects are negligible (Fig. S6).

Fig. S7 presents the selectivity performance of the proposed colorimetric detection system toward catechol in comparison with structurally related phenolic compounds, namely phenol and hydroquinone. At the same concentration, catechol generates a pronounced adsorption band centered around 510 nm, whereas phenol and hydroquinone induce only weak spectral responses over the same wavelength range. The selectivity can be attributed to the *ortho*-dihydroxy structure of catechol, which enables strong coordination with surface metal active sites and facilitates rapid electron transfer during the catalytic oxidation process.[51] In contrast, phenol lacks adjacent hydroxyl groups, while hydroquinone, despite having two hydroxyl groups, adopts a *para*-configuration that is less favorable for chelation

 

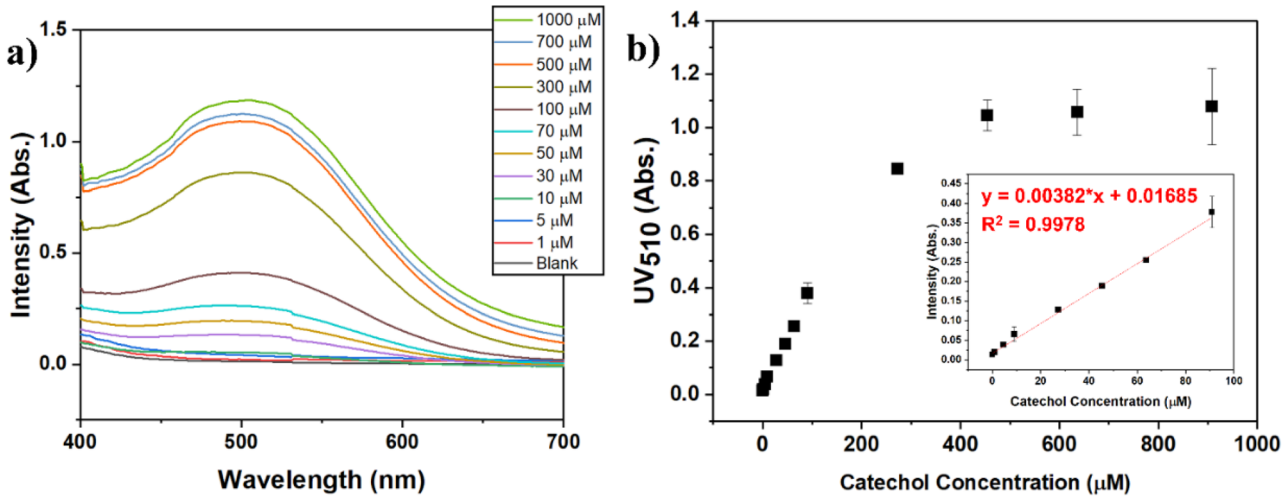


Fig. 6 Calibration curve for catechol detection using MnFeAC (5 : 1): (a) UV-vis absorption spectra showing increasing $UV_{510}$ with rising catechol concentration (1–1000 μM); (b) corresponding calibration plot of $UV_{510}$ *versus* catechol concentration, with the inset highlighting the linear range (1–100 μM) fitted by the regression equation. Experiments were performed in triplicate ($n = 3$). Error bars indicate SD.

and redox cycling on the catalyst surface. Chin *et al.* (2021) mentioned that the reaction between $Fe^{3+}$ and catechol is more pronounced than that with resorcinol and hydroquinone due to the differences in dihydroxy configuration.[51] As a result, the formation of the chromogenic quinone–imine product with 4-AAP is markedly suppressed for these competing phenols.

### 3.5. Proposed mechanism of catechol detection with MnFeAC

The colorimetric detection of catechol using MnFeAC is driven by its oxidase-like catalytic activity, operating in the absence of external activators such as light or $H_2O_2$ and conducted under dark conditions.[16] This highlights the ability of MnFeAC to mediate direct electron transfer between phenolic substrates and dissolved $O_2$, a hallmark of oxidase-like catalysis.

To investigate the roles of reactive oxygen species (ROS) in the detection system, isopropanol (IPA) and ascorbic acid (AA) were employed as scavenging agents for hydroxyl radicals ($^{\bullet}OH$) and superoxide radicals ($O_2^{\bullet-}$), respectively.[2,52] The addition of IPA (1.0 M) did not suppress the colorimetric signal, indicating that $^{\bullet}OH$ do not participate significantly in the reaction. In contrast, AA markedly inhibited the reaction even at low concentration (1 mM) (Fig S8). These results suggested that $O_2^{\bullet-}$ is the predominant radical involved in the system, although electron spin resonance (EPR) is still required to definitively confirm its roles in future studies.[18] Mechanistically, molecular oxygen ($O_2$) can be catalytically activated by MnFeAC to generate reactive oxygen radicals, including hydroxyl radicals ($^{\bullet}OH$) and superoxide radicals ($O_2^{\bullet-}$). These reactive species abstract electrons from the hydroxyl group of catechol, leading to the formation of benzoquinone/benzoquinone radicals. Subsequently, the excess radicals promote the oxidative coupling between 4-AAP and benzoquinone radical to produce the corresponding chromogenic product (Fig. 7).[2,6] The progressive growth of this band under optimized conditions (0.1 mg $mL^{-1}$ MnFeAC, pH 7.4, 40 min, 45 °C) directly correlates with catechol concentration, enabling quantitative detection. Importantly, the reaction proceeds without added oxidants because dissolved molecular oxygen serves as the terminal electron acceptor. The absence of light-driven or peroxide-driven activation underscores that the MnFeAC framework itself provides sufficient redox-through the coupled $Mn^{2+}/Mn^{3+}$ and $Fe^{2+}/Fe^{3+}$ pairs-to sustain electron-transfer network that cycles between reduced and oxidized forms during interaction with dissolved $O_2$ and phenolic substrates. Specifically, $Mn^{2+}$

Table 2 Comparison of colorimetric systems for the detection of phenolic compounds

| Catalyst | Target | Oxidant used | Detection system | $K_m$ (μM) | $V_{max}$ (μM $min^{-1}$) | Linear range (μM) | LOD (μM) | References |
|---|---|---|---|---|---|---|---|---|
| Cu-MOF | Phenol | Dissolved $O_2$ only | 4-AAP | ~200 | ~6.08 | 1–100 | 0.068 | Gao *et al.* (2024)[2] |
| $Cu^{2+}$-MOF | Phenol | Dissolved $O_2$ only | 4-AAP | 150 | 74.40 | 1–200 | 0.061 | Hu *et al.* (2021)[18] |
| ssDNA-AuNPs | Catechol | $Fe^{2+} + H_2O_2$ | | N/A | N/A | 0.2–7.0 | 0.11 | Zhang *et al.* (2016)[15] |
| | Hydroquinone | $Fe^2 + H_2O_2$ | | | | 2.7–19 | 1.6 | |
| Tyr-poly(Ani-*co*-AA) | Catechol | | poly(Ani-*co*-AA) | N/A | N/A | 2.5–50 | 12.3 | Hosu *et al.* (2019)[50] |
| $Co_{1.5}Mn_{1.5}O_4$ | Catechol | Dissolved $O_2$ only | | 12.82 | 4.752 | 1–1000 | 0.35 | Liu *et al.* (2021)[16] |
| GCN-Cu NFs | Catechol | $H_2O_2$ | TMB | 530 | 9.96 | 1–100 | 0.36 | Dang *et al.* (2021)[20] |
| MnFeAC (5 : 1) | Catechol | Dissolved $O_2$ only | 4-AAP | ~379.30 | ~3.4 | 1–100 | 0.87 | This study |

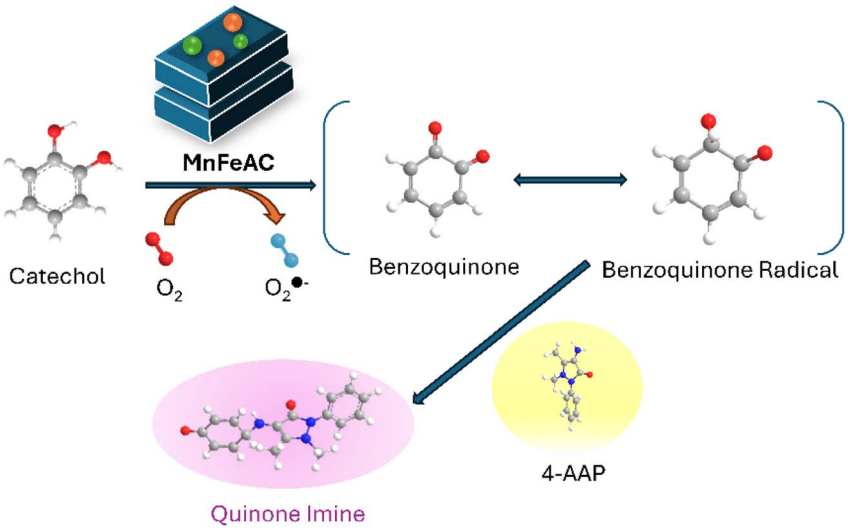


Fig. 7 Proposed mechanism for catechol oxidation catalyzed by MnFeAC.

and $Fe^{2+}$ readily donate electrons to $O_2$, generating $O_2^{\bullet-}$ while forming $Mn^{3+}$ and $Fe^{3+}$ (eqn (6)). Beyond the primary $O_2$-activation step, internal electron exchange between $Mn^{3+}$ and $Fe^{2+}$ provides an additional thermodynamically favorable pathway that regenerates $Mn^{2+}$ without requiring direct reduction by the substrate (eqn (7)). This spontaneous Mn–Fe redox interconversion acts as a redox buffer that stabilizes the mixed valance state and maintains a pool of reduced metal centers capable of activating $O_2$. Besides, the presence of metallic $Mn^0$ and $Fe^0$ within the MnFeAC matrix further reinforces this redox network. Owing to their highly negative redox potential ($E^0 \approx -1.18$ V and $-0.44$ V, respectively), $Mn^0$ and $Fe^0$ can readily undergo surface oxidation in the presence of dissolved $O_2$ to generate $Mn^{2+}/Fe^{2+}$ while reducing $O_2$ to $O_2^{\bullet-}$. These metallic species therefore function as internal electron reservoirs that replenish reduced metal centers, promoting $O_2$ activation, and accelerate the initiation of catalytic cycles (eqn (8)). The oxidized $Mn^{3+}/Fe^{3+}$ species are subsequently reduced back to $Mn^{2+}/Fe^{2+}$ by electron donation from catechol, thereby completing a closed redox loop (eqn (9)).[18]

$$Mn^{2+}/Fe^{2+} + O_2 \rightarrow Mn^{3+}/Fe^{3+} + O_2^{\bullet-} \quad (6)$$

$$Mn^{3+} + Fe^{2+} \rightarrow Mn^{2+} + Fe^{3+} \quad (7)$$

$$Mn^0/Fe^0 + O_2 \rightarrow Mn^{2+}/Fe^{3+} + O_2^{\bullet-} \quad (8)$$

$$Mn^{3+}/Fe^{3+} + \text{catechol} \rightarrow \text{benzoquinone} + Mn^{2+}/Fe^{2+} \quad (9)$$

This dual-valence cycling lowers the activation barriers for $O_2$ activation, accelerates substrate oxidation, and prevents catalyst deactivation by continuously regenerating active sites. Collectively, this intrinsic oxidase-like mechanism explains the reproducible detection of catechol observed across varying Mn : Fe ratios and operating conditions.

## 4. Conclusion

In this study, MnFe aminoclay (MnFeAC) was demonstrated to exhibit intrinsic oxidase-like activity involving $O_2^{\bullet-}$ as the dominant reactive species, enabling the colorimetric detection of catechol through the formation of a quinone–imine dye with a characteristic absorbance at ~510 nm. Systematic optimization revealed that a catalyst dosage of 0.10 mg $mL^{-1}$, pH 7.4, a reaction time of 40 min, and a temperature of 45 °C provided the most favorable conditions for sensitive and reproducible detection. Under these parameters, the system achieved a linear response in the range of 1–100 μM catechol, with an LOD of 0.87 μM and an LOQ of 2.62 μM. Importantly, the catalytic process proceeded in the dark and without the addition of external oxidants such as $H_2O_2$, relying solely on dissolved $O_2$ as the electron acceptor. This peroxide-free design represents a safer and more environmentally friendly approach compared to many previously reported colorimetric systems.

Nevertheless, several limitations of this work must be acknowledged. The detection limits, while sufficient for proof-of-concept, remain higher than those achieved by enzyme-based assays or certain nanozyme systems. In addition, the study was limited to a small set of phenolic compounds (catechol, phenol, and hydroquinone). The response of the detection system to other phenolic compounds should be investigated in future work. EPR measurements should also be performed to verify the roles of $O_2^{\bullet-}$. Finally, the performance of the system should be evaluated under atmosphere-controlled ($N_2/O_2$) conditions to provide direct evidence for the involvement of dissolved oxygen.

Overall, this work serves as a preliminary demonstration of MnFeAC as an oxidase mimic for phenolic detection. Future studies should aim to improve sensitivity through material modification, expand the substrate scope to diverse phenolic pollutants, and validate the system under real-sample conditions. Integration with portable colorimetric platforms or

paper-based devices may further enhance its applicability in environmental monitoring and biosensing.

## Author contributions

Hai Le Tran: writing – original draft, writing – review & editing, methodology, visualization, investigation; Kieu Tran Thi Thuy: writing – review & editing, investigation; Luan Thanh Nguyen: writing – review & editing; Viet Quoc Nguyen: writing – review & editing; Tin Chanh Duc Doan: writing – review & editing; Van-Quy Hoang: writing – review & editing; Thi H. Ho: writing – review & editing; Vu Khac Hoang Bui: writing – original draft, writing – review & editing, methodology, investigation, visualization, conceptualization.

## Conflicts of interest

There are no conflicts to declare.

## Data availability

All data of this study are available within the paper and its supplementary information (SI). Supplementary information: SEM–EDS elemental mapping analysis, $N_2$ desorption isotherm and BJH pore structrure analysis, Michealis–Menten kinetic analysis, effect of $H_2O_2$ on reaction time, storage ability of MnFeAC, effect of common inorganic ions on $UV_{510}$, UV-vis adsorption spectra of catechol, phenol, and hydroquinone, $UV_{510}$ response of detection system in the presence of scavenging agents, specific surface area (BET), pore size, and pore volume of MnAC, FeAC, and MnFeAC (5 : 1), and recovery analysis of catechol in tap water. See DOI: https://doi.org/10.1039/d5ra07889j.

## Funding

The Vietnam National Foundation for Science and Technology Development (NAFOSTED) under grant number "104.02-2023.102"

## Acknowledgements

This research was supported by the Vietnam National Foundation for Science and Technology Development (NAFOSTED) under grant number "104.02-2023.102". The author thanks Key Laboratory for Polymer and Composite Materials, Viet Nam National University Ho Chi Minh City for their support to carry out this work.

## Notes and references

1 N. Xing, Y. Lyu, J. Li, D. H. L. Ng, X. Zhang and W. Zhao, *J. Hazard. Mater.*, 2023, **442**, 129914.
2 Z. Gao, J. Guan, M. Wang, S. Liu, K. Chen, Q. Liu and X. Chen, *Talanta*, 2024, **272**, 125840.
3 K.-G. Fahlbusch, F.-J. Hammerschmidt, J. Panten, W. Pickenhagen, D. Schatkowski, K. Bauer, D. Garbe and H. Surburg, *Ullmann's Encycl. Ind. Chem.*, 2003, DOI: 10.1002/14356007.a11_141.
4 H. Fiege, H.-W. Voges, T. Hamamoto, S. Umemura, T. Iwata, H. Miki, Y. Fujita, H.-J. Buysch, D. Garbe and W. Paulus, *Ullmann's Encycl. Ind. Chem.*, 2000, DOI: 10.1002/14356007.a19_313.
5 S. Suresh, V. C. Srivastava and I. M. Mishra, *Int. J. Energy Environ. Eng.*, 2012, **3**, 32.
6 S. Wu, D. Guo, X. Xu, J. Pan and X. Niu, *Sens. Actuators, B*, 2020, **303**, 127225.
7 S. Li, K. Sun, A. Latif, Y. Si, Y. Gao and Q. Huang, *Environ. Sci. Technol.*, 2022, **56**, 7412–7425.
8 J. Dec, K. Haider and J.-M. Bollag, *Chemosphere*, 2003, **52**, 549–556.
9 S. Dubey, D. Singh and R. A. Misra, *Enzyme Microb. Technol.*, 1998, **23**, 432–437.
10 L. Yuan, J. Chai, S. Wang, T. Li, X. Yan, J. Wang and H. Yin, *Environ. Technol. Innovation*, 2023, **30**, 103085.
11 V. K. H. Bui, H. B. Truong, S. Hong, X. Li and J. Hur, *J. Clean. Prod.*, 2023, **402**, 136832.
12 R. Lv, S. Sun, K. Wang, Y. A. Golubev, F. Dong, O. B. Kotova, J. Liu, M. Liu and D. Tan, *J. Mater. Sci.*, 2022, **57**, 10084–10099.
13 Y. Zeng, S. Sun, R. Lv, K. Wang, Y. A. Golubev, S. Lin, F. Dong, E. L. Kotova and O. B. Kotova, *J. Environ. Chem. Eng.*, 2024, **12**, 111771.
14 Y. Lu, X. Zhang and Y. Huang, *Chin. Chem. Lett.*, 2025, **36**, 110129.
15 L. P. Zhang, Y. P. Xing, L. H. Liu, X. H. Zhou and H. C. Shi, *Sens. Actuators, B*, 2016, **225**, 593–599.
16 X. Liu, J. Yang, J. Cheng, Y. Xu, W. Chen and Y. Li, *Sens. Actuators, B*, 2021, **337**, 129763.
17 X. Liu, X. Cao, S. Zhao, Z. Liu, G. Lu and Q. Liu, *Anal. Methods*, 2021, **13**, 5377–5382.
18 C. Y. Hu, Z. W. Jiang, C. Z. Huang and Y. F. Li, *Microchim. Acta*, 2021, **188**, 1–8.
19 C. Ding, Y. Zhu, Z. Huo, S. Yang, Y. Zhou, A. Yiming, W. Chen, S. Liu, K. Qian and L. Huang, *Mater. Today Bio*, 2024, **26**, 101047.
20 T. V. Dang, N. S. Heo, H.-J. Cho, S. M. Lee, M. Y. Song, H. J. Kim and M. I. Kim, *Microchim. Acta*, 2021, **188**, 293.
21 K. K. R. Datta, A. Achari and M. Eswaramoorthy, *J. Mater. Chem. A*, 2013, **1**, 6707–6718.
22 A. A. Jeya Ranchani, V. Parthasarathy, C. Hu, Y. F. Lin, K. L. Tung and R. Anbarasan, *Chem. Eng. Commun.*, 2020, **207**, 871–886.
23 S. I. Sanakal, A. Das, A. Babu, P. Kar, V. Nutalapati, K. K. R. Datta, S. Banerjee and S. Maji, *J. Environ. Chem. Eng.*, 2025, **13**, 115398.
24 M. A. Ganayee, C. K. Manju, W. A. Dar, B. Mondal and T. Pradeep, *Ind. Eng. Chem. Res.*, 2020, **59**, 12737–12744.
25 Y. J. Jang, V. K. H. Bui, P. T. Nguyen, Y.-C. Lee and M. I. Kim, *Chemosensors*, 2021, **9**, 219.
26 H. P. Song, Y. Lee, V. K. H. Bui, Y.-K. Oh, H. G. Park, M. I. Kim and L. Young-Chul, *Sensors*, 2018, **18**, 457.
27 V. K. H. Bui, J.-S. Koh, H. U. Lee, D. Park and Y.-C. Lee, *Mater. Chem. Phys.*, 2022, **290**, 126541.

28 T. Zhou, Z. Liu and T. Yu, *Ind. Eng. Chem. Res.*, 2024, **63**, 12806–12814.
29 T. N. Pham, N. Thi Hue, Y. C. Lee, T. Q. Huy, N. Thi Thu Thuy, H. V. Tuan, N. T. Khi, V. N. Phan, T. D. Thanh, V. D. Lam and A. T. Le, *RSC Adv.*, 2021, **11**, 38578–38588.
30 K. N. Mahadevaprasad, K. N. Santhosh, S. V. Kamath and S. K. Nataraj, *Chemosphere*, 2024, **366**, 143480.
31 A. S. Kaloudi, A. M. Athinodorou, K. Spyrou, Y. V. Simos, P. Zygouri, M. A. Hammami, K. K. R. Datta, P. Vezyraki, D. Peschos, K. Tsamis and D. P. Gournis, *Appl. Mater. Today*, 2023, **35**, 102006.
32 T. Ameh and C. M. Sayes, *Environ. Toxicol. Pharmacol.*, 2019, **71**, 103220.
33 R. Fu, Y. Hu, X. Liu, H. He and J. Yi, *Chem. Eng. J.*, 2025, **512**, 162299.
34 W. Tan, R. Xin, J. Zhang, L. Yang, M. Jing, F. Ma and J. Yang, *Materials*, 2023, 16.
35 J. Uhrovčík, *Talanta*, 2014, **119**, 178–180.
36 P. Guo and C. Wang, *RSC Adv.*, 2017, **7**, 4437–4443.
37 Q. Chang, J. Li, H. Suo, M. Qing, H. Wang, C. Zhang, X. Wen, H. Xiang, Y. Yang and Y. Li, *Catal. Today*, 2024, **431**, 114605.
38 R. Tholkappiyan, A. N. Naveen, K. Vishista and F. Hamed, *J. Taibah Univ. Sci.*, 2018, **12**, 669–677.
39 L. Guo, J. Sun, X. Ji, J. Wei, Z. Wen, R. Yao, H. Xu and Q. Ge, *Commun. Chem.*, 2018, **1**, 11.
40 M. Ramadan, A. M. Abdellah, S. G. Mohamed and N. K. Allam, *Sci. Rep.*, 2018, **8**, 7988.
41 Y. Zhong, X. Qiu, J. Gao and Z. Guo, *ISIJ Int.*, 2019, **59**, 1098–1104.
42 Y. Kuwahara, G. Kato, A. Fujibayashi, K. Mori and H. Yamashita, *Chem.–Asian J.*, 2020, **15**, 2005–2014.
43 R. Huang, M. Tang, W. Kan, H. Xu, K. Wu, Z. Wang and H. Li, *J. Phys. D: Appl. Phys.*, 2024, **57**, 015102.
44 Š. Meškinis, A. Vasiliauskas, M. Andrulevičius, D. Peckus, S. Tamulevičius and K. Viskontas, *Materials*, 2020, **13**, 1003.
45 P. Cheng, Y. Li, Y. Ma, C. Qiu, T. Fu, Y. Wang and F. Wu, *Molecules*, 2025, **30**, 2325.
46 M. C. Biesinger, B. P. Payne, A. P. Grosvenor, L. W. M. Lau, A. R. Gerson and R. S. C. Smart, *Appl. Surf. Sci.*, 2011, **257**, 2717–2730.
47 J. Aluha, S. Blais and N. Abatzoglou, *Catal. Lett.*, 2018, **148**, 2149–2161.
48 J. K. Tripathi, M. Garbrecht, W. D. Kaplan, G. Markovich and I. Goldfarb, *Nanotechnology*, 2012, **23**, 495603.
49 R. Oro, M. Campos, E. Hryha, J. M. Torralba and L. Nyborg, *Mater. Charact.*, 2013, **86**, 80–91.
50 O. Hosu, M. Lettieri, N. Papara, A. Ravalli, R. Sandulescu, C. Cristea and G. Marrazza, *Talanta*, 2019, **204**, 525–532.
51 H. Chin, K. S. Hopstock, L. T. Fleming, S. A. Nizkorodov and H. A. Al-Abadleh, *Environ. Sci.: Atmos.*, 2021, **1**, 64–78.
52 M. S. Khan, M. Khalid, M. S. Ahmad, M. Shahid and M. Ahmad, *Res. Chem. Intermed.*, 2020, **46**, 2985–3006.